

# Interpretable Deep Learning for Pattern Recognition in Brain Differences Between Men and Women

Maxim Kan<sup>1</sup>, Ruslan Aliev<sup>1</sup>, Anna Rudenko<sup>1</sup>, Nikita Drobyshev<sup>1</sup>, Nikita Petrashen<sup>1</sup>, Ekaterina Kondrateva<sup>1</sup>, Maxim Sharaev<sup>1</sup>, Alexander Bernstein<sup>1</sup>, and Evgeny Burnaev<sup>1</sup>

Skolkovo Institute of Science and Technology, Moscow, Russia

**Abstract.** Deep learning shows high potential for many medical image analysis tasks. Neural networks work with full-size data without extensive preprocessing and feature generation and, thus, information loss. Recent work has shown that morphological difference between specific brain regions can be found on MRI with deep learning techniques. We consider the pattern recognition task based on a large open-access dataset of healthy subjects — an exploration of brain differences between men and women. However, interpretation of the lately proposed models is based on a region of interest and can not be extended to pixel or voxel-wise image interpretation, which is considered to be more informative. In this paper, we confirm the previous findings in sex differences from diffusion-tensor imaging on T1 weighted brain MRI scans. We compare the results of three voxel-based 3D CNN interpretation methods: Meaningful Perturbations, GradCam and Guided Backpropagation and provide the open-source code.

**Keywords:** MRI · Neural Networks · Deep Learning · 3D CNN · CNN interpretation · Meaningful perturbation · GradCam

## 1 Introduction

Deep learning recently has found many applications in the area of medical diagnostics/image processing [21] [17]. For example, processing Magnetic Resonance Images (MRI) using a convolutional neural network (CNN) allows to reduce the dose of gadolinium used for contrast by an order of magnitude. [10]. Another example is detection of cerebral microbleeds using a 3D-CNN [6]. Tissue segmentation in MR images plays a great importance in modern medical research. One of the most common image segmentation tasks in brain MRI is the segmentation of Gray Matter (GM), White Matter (WM), and Cerebrospinal Fluid (CSF). One possible approach to this segmentation task is proposed in [29]. The authors apply convolutional networks to multi-modal (T1, T2 and FA) MRI images in order to segment infant brain tissue images into GM, WM, and CSF. CNNs are applied to a variety of regression tasks, see [18]. Finally,

CNNs are used in early-stage Alzheimer’s disease detection in MRI and PET images [24]. Conventionally, the brain data is firstly processed to get the lower dimensional meaningful features [14], for diffusion tensor imaging (DTI) — it is fraction anisotropy (FA), mean diffusivity (MD), axial diffusivity (AD), and radial diffusivity (RD) values [27]. For functional T2\* MRI images it is functional connectivity features, spectral features and etc. Classifier constructions follows this feature extraction step. However, deep learning approaches, especially those for processing 3D data, are shown to be more accurate in many applications [27] as they use full-sized data without information loss during extensive preprocessing. Working on deep learning models interpretation in MRI implies training on large databases of healthy subjects. One of the most common and highly explored databases available in open-access is Human Connection Project (HCP)<sup>1</sup>. A conventional task being extensively explored on this database is a task of sex patterns recognition between men and women.

Men and women do a lot of things like encoding memories, sensing emotions, recognizing faces, solving certain problems, and making decisions in different ways. Since the brain controls cognition and behaviors, these sex-related functional differences may be associated with the gender-specific structure of the brain [5]. Also recent studies indicate that gender may affect the human cognitive functions, such as emotion, memory, perception and etc. [3].

However, previous studies on morphological difference between specific brain regions show interpretation only on the feature or region-of-interest level. On the contrary, the state-of-the-art deep-learning interpretation methods allow visualisation of the decision rule in a pixel-wise fashion [27]. Or in the case of 3D convolution models — voxel-wise [16]. The contributions of the proposed paper are as follows:

- we reproduce the state-of-the-art 3D CNN model [27] to investigate the difference between men and women brains on T1 images and confirm previous findings on DTI;
- we are first, to the best of our knowledge, to apply several network interpretation methods to the 3D CNN model: Meaningful Perturbations, GradCam and Guided Backpropagation to find sex specific patterns and compare there performances.
- we compare these results to the conventional machine learning classification models on morphometry data of the same subjects.

The source code is open and available at <https://github.com/maxs-kan/InterpretableNeuroDL>

## 2 Data

The database Human Connectome Project (HCP) contains MRI data from 1113 subjects, including 507 men and 606 women. We explored T1 images, preprocessed with HCP- pipelines<sup>2</sup>.

<sup>1</sup> <https://db.humanconnectome.org>

<sup>2</sup> <https://github.com/Washington-University/HCPpipelines>

For the morphometry data analysis we used Freesurfer <sup>3</sup> preprocessed features from section **Expanded FreeSurfer Data** for the same 1113 subjects. The morphometry characteristics (volumes, surface areas, thicknesses, etc.) are calculated for 34 cortical regions according to Desikan-Killiany Atlas and for 45 subcortical areas according to Automatic subcortical segmentation [8] resulting in a vector of 935 features for each subject.

### 3 Methods

#### 3.1 Morphometry data analysis and interpretation

We used the morphometry data classification as a baseline machine learning model. The best performing model is chosen among different classifiers (XG-Boost, k-Nearest Neighbors(KNN) and Logistic Regression) via a grid-search. All considered models were validated with 10-fold cross-validation technique and most important features were chosen with the model feature scoring.

#### 3.2 Full-size data analysis: 3D CNN

In this work we used state-of-the-art 3D CNN model architecture from the [27].

The neural network consists of three hidden layers, a linear layer, which integrates the output of the hidden layers into the inputs of the terminal softmax activation layer. The first layer is a convolutional layer which convolves the input tensor with a kernel. The size of the kernel is  $3 \times 3 \times 3$  for all three hidden layers. After each convolutional layer we used batch normalization to normalize the data of each mini-batch. Then we go with activation Re-LU layer, Dropout layer, Pooling layer with max-pooling method to summarize the outputs of neighboring groups of neurons in the same kernel map, which halves the size of data in each dimension. To compare results with standard ML methods, we trained Support Vector Machine classifier on MRI data, with flattening MRI 3D tensors into 1-dimensional vector.

We used cross-entropy loss for training and Adam optimizer with learning rate  $\alpha = 0.0003$ ,  $L_2$  regularization of  $\lambda = 10^{-6}$ , exponential decay rates for the moment estimates  $\beta_1 = 0.9$ ,  $\beta_2 = 0.999$ ,  $\varepsilon = 10^{-8}$ . Also, we used scheduler strategy, which reduces stepsize as epoch increases, and early stopping to prevent overfitting. Batch size for training is set to 45.

Due to low amount of data, we performed 10-fold cross-validation to estimate model performance (stratified strategy).

We compared the results of the 3D CNN network to the support vector machine classifier with *rbf* kernel (SVM) results, trained on the full size data reshaped to the 1-dimensional vector, as proposed in [27].

---

<sup>3</sup> <https://surfer.nmr.mgh.harvard.edu/>

### 3.3 3D CNN interpretation

**Feature Analysis in the First Hidden Layer of 3D CNN.** We analyzed features in the first hidden layer, as they are less abstractive [27], and can represent the structural features of MRI images. There are 32 features after the first hidden layer, according to the proposed architecture.

Firstly, we computed mean of voxel values for each feature for men and women with confidence intervals. We used two-sample t-test to determine significant difference among these values.

Secondly, for each individual we normalized feature map, so all elements are integers in range  $[0, 255]$ , and computed entropy values for each individual with formula:

$$H = - \sum_{i=0}^{255} p_i \cdot \log p_i, \quad (1)$$

where  $p_i$  shows how often a pixel with value  $i$  appears in the image.

**Meaningful Perturbations for 3D CNN results interpretation.** The goal of the method [9] is to perturb the smallest possible region of the MRI such that the model significantly changes its output probability for MR image class, which means that this region is the most important for model decision and it is the most informative part of the image. In this work we perturb original image  $x_0$  by replacing the corresponding region with Gaussian blurring of the image. Let  $m : \Lambda \rightarrow [0, 1]$  be a mask associating each voxel  $u \in \Lambda$  of input image with scalar value  $m(u)$ . Then the perturbation operator:

$$P(x_0; m) = x_0 \odot m + (g_{\sigma_0} * x_0) \odot (1 - m) \quad (2)$$

and  $g_{\sigma_0}$  is a 3D Gaussian kernel. Our goal is to find the smallest deletion mask  $m$  that causes the score  $f_c(P(x_0; m)) \ll f_c(x_0)$ , where  $f_c(\cdot)$  is the probability of belonging to a class  $c$ . To avoid the artifacts [13], we pad the  $x_0$  with  $j$  zeros and the mask  $m$  applied to  $x_0^K$ :

$$x_0^K = x_0[K : H + j + K, K : W + j + K, K : D + j + K] \quad (3)$$

with integer  $K$  drawing from the discrete uniform distribution on  $[0, j]$ , where  $H, W, D$  - size of image. Also, to obtain a mask more representative of natural perturbations, we can encourage it to have a simple structure. We do so by regularizing  $m$  in total-variation (TV) norm, upsampling it by factor  $s$  to image size from a low resolution version and applying Gaussian filter on the upsampling mask. Let us denote by  $M = g_{\sigma_m} * (Up(m, s))$ , where  $g_{\sigma_m}$  is a 3D Gaussian kernel and  $Up(\cdot, s)$  is a trilinear upsampling algorithm by factor of  $s$ . Finding  $m_c$  for class  $c$  can be formulated as the following optimization problem:

$$m_c = \arg \min_m \mathbb{E}_{K \sim U[0, j]} (f_c(P(x_0^K, M)) + \lambda_2 \sum_u \|\nabla M(u)\|^\beta + \lambda_1 \|1 - m\|_1) \quad (4)$$

For our experiment  $\sigma_0 = \sigma_m = 10$ ,  $\lambda_1 = 3$ ,  $\lambda_2 = 1$ ,  $\beta = 7$ ,  $s = 4$ ,  $j = 5$ , and repeat jittering 10 times. The score is optimized by Adam optimizer with learning rate  $\alpha = 0.3$ , exponential decay rates for the moment estimates  $\beta_1 = 0.9$ ,  $\beta_2 = 0.99$ .

**Guided Backpropagation for 3D CNN results interpretation.** In order to obtain saliency maps of an input MRI from our network we use Guided Backpropagation method [23]. This approach computes the gradient of the score for class  $c$ ,  $y^c$ , with respect to the input image  $x$ :

$$m_c = \frac{dy^c}{dx}. \quad (5)$$

The gradient computed with specific backpropagation through the ReLU non-linearity. In Guided Backpropagation, we backpropagated the positive values of the gradient and set the negative ones to zero. And as usual, we backpropagated values of the gradient, which corresponds to positive values of the input to ReLU. Let  $G^l$  be a gradient backpropagated through layer  $l$  and  $f_i^{l+1} = \text{ReLU}(f_i^l)$ :

$$G_i^l = (f_i^l > 0) \cdot (G_i^{l+1} > 0) \cdot G_i^{l+1}. \quad (6)$$

**GradCAM for 3D CNN results interpretation.** GradCAM [20] interprets the model, assuming that the deep CNN layers capture higher-level visual constructs [4]. In these layers neurons attends to the parts of the objects which responsible for the class. GradCAM computes the gradient for score  $y^c$  of class  $c$  before terminal layer with respect to filter activations of the last convolutional layer  $F^k$ . Then it computes the importance weights for each filter, i.e.

$$\alpha_k^c = \frac{1}{H \cdot W \cdot D} \sum_{i=1}^H \sum_{j=1}^W \sum_{k=1}^D \frac{\partial y^c}{\partial F_{i,j,k}^k}, \quad (7)$$

where  $H, W, D$  — size of a filter activation tensor.  $\alpha_k^c$  captures the “importance” of filter  $k$  for a target class  $c$ . To obtain the class-discriminative localization mask  $m_c$ , we computed a weighted combination of filter activations, and follow it by a ReLU:

$$m_c = \text{ReLU} \left[ \sum_{k=1} \alpha_k^c \cdot F^k \right]. \quad (8)$$

Also we upsampled  $m_c$  to the input image resolution using trilinear interpolation.

## 4 Results

### 4.1 Morphometry data

The results of 10-folds cross-validation for 1113 subjects are in Table 1 and feature importances ( $\beta$  scores) for Logistic Regression model chosen via a grid search are represented on Fig. 1.

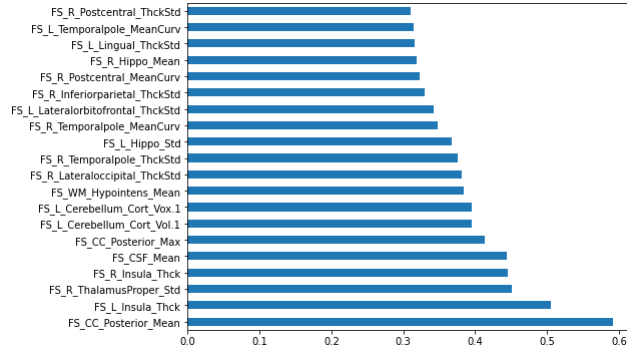


**Fig. 1.** Feature importances for Logistic Regression model.

**Table 1.** Results for baseline morphometry data classification models: 10-fold cross-validation

	XGB	KNN	Logistic regression
Mean accuracy	0.89	0.85	0.92
STD	0.02	0.04	0.03

As can be seen from Fig. 1, the most important features for the Logistic Regression model belong to the following brain regions volumes and intensities: corpus callosum, left and right insula and thalamic regions, as well as whole brain metrics for white matter hyperintensities and intensity of cerebrospinal fluid.

## 4.2 3D CNN model results

The 3D CNN model with the proposed architecture yields the mean accuracy of  $0.92 \pm 0.03$  on 10-fold cross-validation. SVM achieves  $0.90 \pm 0.02$  accuracy on 10-fold cross-validation. So 3D-CNN model slightly outperforms standard SVM.

## 4.3 Feature Analysis in the First Hidden Layer of 3D CNN

We analyzed features in the first hidden layer. Mean voxel values for 31 features have significant difference in men-women groups, with 10 features larger for women, and 21 features larger for men (see Fig. 2).

The structural features extracted from 3D CNN reflect the brain structure differences between men and women. In the first hidden layer of 3D CNN model, we have found 25 features that have significant difference between men and women in voxels value. Moreover, using entropy measure, we found a range of features with higher complexity in a men’s brain as reflected by significantly higher entropy value. These results indicate that the gender-related differences are likely to exist in the whole-brain range including both white and gray matter. We would like to highlight that these results are in line with the previous results

from [27], where the authors showed on the same dataset that the men’s brain have more complex features, and thus, higher entropy.

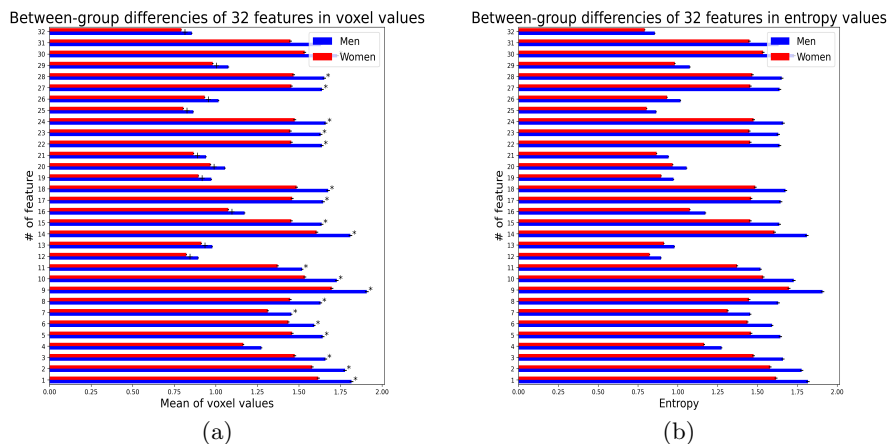


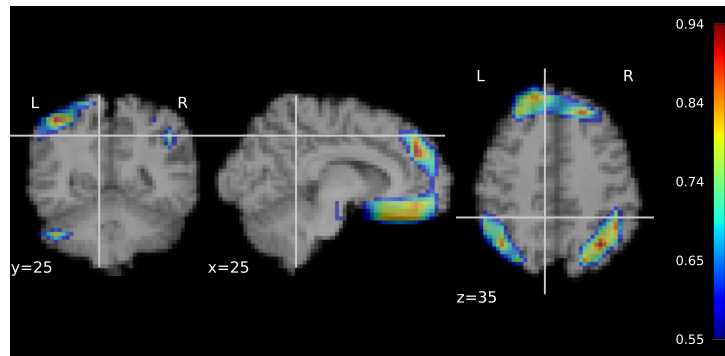
**Fig. 2.** (a) Mean voxel values for each feature in male/female groups. Features that are significantly large for men are marked with \*, features that are significantly large for women are marked with +. (b) Mean entropy values for each feature in male/female groups.

#### 4.4 Meaningful Perturbations for 3D CNN

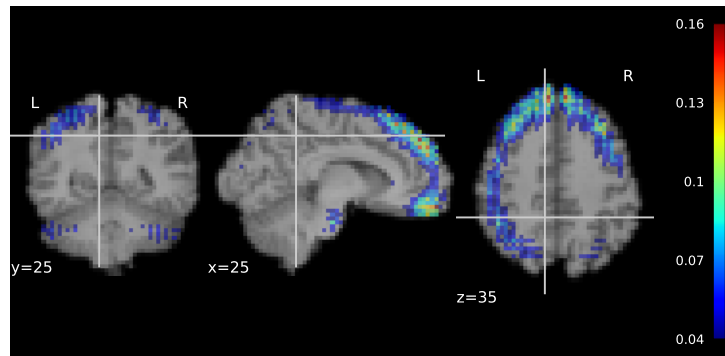
For the two target classes in the sex differences classification, we get two different feature maps correspondingly with the meaningful perturbations algorithm. Two feature masks for men and women appear to highlight different regions of interest, and were then explored separately.

We completed 10 fold cross validation to check the 3D CNN performance with the images restricted on masks. Then we multiplied every validation sample by average male mask, by average female mask or by the sum of these masks voxel-wise. The accuracy for the male mask is  $0.56 \pm 0.13$ , for the female mask —  $0.63 \pm 0.09$  and for the conjoined mask —  $0.81 \pm 0.11$  respectively. Thus, we can conclude that all necessary information for classification problem is both in male and female masks (in their conjunction). The difference in masks for male and female may be explained by the specifics of the algorithm: we need to find the smallest region in the input image, deletion of which will decrease the probability of being a specific class. In Fig. 3a we show the final mask which contains regions for men and women.

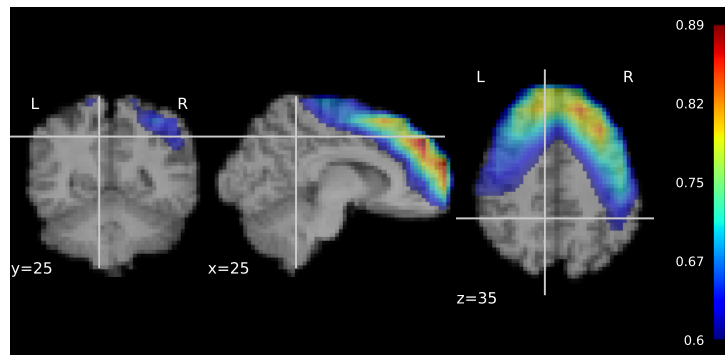
Next, we segmented each MR image into 246 gray matter regions according to the Human Brainnetome Atlas [7], and 50 white matter regions according to the ICBM-81 White-Matter Labels Atlas [15]. For each region of each brain atlas,



(a)



(b)



(c)

**Fig. 3.** Cross-sectional view on three attention maps for 3D CNN interpretation obtained with: a. Meaningful Perturbation (conjoined male and female attention mask), b. Guided Backpropagation, c. GradCAM. The greater the voxel's value of each mask, the more important this voxel for classification.

we estimated fractions of voxels of this region included into the mask, which we have obtained via Meaningful Perturbations. We normalized these fractions, so the values for all regions would sum up to 1. The top-5 scored regions of each atlas with the largest values as proposed in [27] are presented in Table 2.

**Table 2.** The most discriminative regions of each atlas obtained with Meaningful Perturbations method.

ICBM White-Matter Labels Atlas	
Regions	Score
Corticospinal tract right	0.1273
Corticospinal tract left	0.0927
Anterior corona radiata right	0.0594
Pontine crossing tract	0.0580
Cerebral peduncle left	0.0488

Human Brainnetome Atlas	
Regions	Male score
OrG_R_6_5	0.0131
OrG_R_6_3	0.0124
IPL_R_6_2	0.0120
MFG_R_7_1	0.0118
PhG_L_6_5	0.0117

These findings partially overlap with the morphometry results, showing common white matter regions in the corpus callosum (Anterior corona radiata), as well as cerebellum (Cerebral peduncle). The gray matter region in common overlaps on frontal gyri (MFG\_R).

#### 4.5 Guided Back-propagation for 3D CNN

We computed a saliency map for every person in the dataset and then took mean over the dataset. As we have two classes in our dataset, the final map contains the regions of interest for each class, see Figure 3b.

#### 4.6 GradCAM for 3D CNN

We compute corresponding localization masks, containing information about both male and female regions of interest. The cross-sectional view of the result is shown on 3c.

## 5 Conclusion

We reproduced the state-of-the-art 3D CNN model from [27] DTI study and found similar differences on MRI T1w images. The model exhibits the mean

accuracy of  $0.92 \pm 0.03$ , which is slightly higher than morphometry data classification having less variance. We are the first, to the best of our knowledge, to apply several network interpretation methods to the 3D CNN model: Meaningful Perturbations, GradCam and Guided Backpropagation to find gender specific patterns, and to compare their performances. We observed similar results, which means that the masks computed with all three methods reveal similar patterns and thus are trustworthy. We found that GradCam method is the fastest one and ready plug-and-play method, while the Meaningful Perturbations method is slowest one yet showing most anatomic-like attention maps. Our deep learning results are in line with conventional machine learning classification model results on morphometric data. We also publish the code to the open-source library for public use. The proposed interpretation tool could be successfully used in various MRI pathology detection applications like epilepsy detection, Alzheimer disorder diagnosis, Autism Spectrum disorder classification and others.

## 6 Discussion

In the current work we aimed at studying sex-related differences in human brain.

In order to localize the most informative brain areas for classification task, we created attention maps for 3D CNN output in three different ways. Using these maps we were able to denote which brain regions play the most important role in the sex classification task. For men the brain region with the highest classification accuracy was Parietal Lobe, namely Superior parietal lobule and Inferior parietal lobule (Brodmann areas 5 and 7) in line with the previous studies [19], where it was shown that parietal lobe activity is biased to the right hemisphere in men. Comparing this result to the [27] we can notice that the region with higher classification accuracy in their study — left precuneus (BA 31) — is bounded cytoarchitecturally with superior and inferior parietal lobules so we may suppose gender structural differences in this region. Moreover, the Medial frontal gyrus (part of parietal Lobe as well, BA 6,8,10,46) contributed significantly to the classification task. It could be explained by the morphological asymmetry of the medial frontal gyrus in the men brain [22].

Female brain analysis shows different brain regions with high classification accuracy. In line with the previous study [27] we detected orbital gyrus (BA 13, 14) to be essential in sex detection. Moreover, in female brain parahippocampal gyrus also appears to affect the classification accuracy. Our results show that Amygdala and Hippocampus (part of Subcortical nuclei) turned out to be regions of high classification accuracies though previous studies show that both these regions are not sexually dimorphic [25] [12].

In white matter we found the following regions in the male brain with the highest classification accuracy: cingulate gyrus, middle cerebellar peduncle, Anterior corona radiata left, Posterior thalamic radiation, corpus collosum. Which is in line with previous studies [26], [1].

We also found that middle cerebellar peduncle is informative for classification task, which is in line with the previous studies [11]. Cingulate gyrus as well as

Posterior thalamic radiation were both detected to have sex differences [2]. We also found the regions in limbic-thalamo-cortical circuitry which exhibit gender-related differences (cingulate gyrus and Anterior corona radiata), which also coincides with the results of the previous study [27].

It is also worth noting, that attention maps in Fig. 3a show the spatial pattern of frontoparietal resting-state brain network, which was initially discovered from resting-state fMRI activity and is thought to be involved in a wide variety of tasks by initiating and modulating cognitive control abilities [28]. It might be interesting in future research to look specifically at this network and explore it in terms of gender-related brain differences.

## References

1. Bava, S., Boucquey, V., Goldenberg, D., Thayer, R.E., Ward, M., Jacobus, J., Tapert, S.F.: Sex differences in adolescent white matter architecture. *Brain research* **1375**, 41–48 (2011)
2. Brun, C.C., Lepore, N., Luders, E., Chou, Y.Y., Madsen, S.K., Toga, A.W., Thompson, P.M.: Sex differences in brain structure in auditory and cingulate regions. *Neuroreport* **20**(10), 930 (2009)
3. Cahill, L.: Why sex matters for neuroscience. *Nature reviews neuroscience* **7**(6), 477–484 (2006)
4. Chen, X., Fang, H., Lin, T.Y., Vedantam, R., Gupta, S., Dollár, P., Zitnick, C.L.: Microsoft coco captions: Data collection and evaluation server. *arXiv preprint arXiv:1504.00325* (2015)
5. Cosgrove, K.P., Mazure, C.M., Staley, J.K.: Evolving knowledge of sex differences in brain structure, function, and chemistry. *Biological psychiatry* **62**(8), 847–855 (2007)
6. Dou, Q., Chen, H., Yu, L., Zhao, L., Qin, J., Wang, D., Mok, V.C., Shi, L., Heng, P.A.: Automatic detection of cerebral microbleeds from mr images via 3d convolutional neural networks. *IEEE transactions on medical imaging* **35**(5), 1182–1195 (2016)
7. Fan, L., Li, H., Zhuo, J., Zhang, Y., Wang, J., Chen, L., Yang, Z., Chu, C., Xie, S., Laird, A.R., et al.: The human brainnetome atlas: a new brain atlas based on connectonal architecture. *Cerebral cortex* **26**(8), 3508–3526 (2016)
8. Fischl, B.: Freesurfer. *Neuroimage* **62**(2), 774–781 (2012)
9. Fong, R.C., Vedaldi, A.: Interpretable explanations of black boxes by meaningful perturbation. In: *Proceedings of the IEEE International Conference on Computer Vision*. pp. 3429–3437 (2017)
10. Gong, E., Pauly, J.M., Wintermark, M., Zaharchuk, G.: Deep learning enables reduced gadolinium dose for contrast-enhanced brain mri. *Journal of Magnetic Resonance Imaging* **48**(2), 330–340 (2018)
11. Kanaan, R.A., Chaddock, C., Allin, M., Picchioni, M.M., Daly, E., Shergill, S.S., McGuire, P.K.: Gender influence on white matter microstructure: a tract-based spatial statistics analysis. *PLoS One* **9**(3) (2014)
12. Kret, M.E., De Gelder, B.: A review on sex differences in processing emotional signals. *Neuropsychologia* **50**(7), 1211–1221 (2012)
13. Kurakin, A., Goodfellow, I., Bengio, S.: Adversarial examples in the physical world. *arXiv preprint arXiv:1607.02533* (2016)

14. Lasič, S., Szczepankiewicz, F., Eriksson, S., Nilsson, M., Topgaard, D.: Microanisotropy imaging: quantification of microscopic diffusion anisotropy and orientational order parameter by diffusion mri with magic-angle spinning of the q-vector. *Frontiers in Physics* **2**, 11 (2014)
15. Mori, S., Wakana, S., Nagae-Poetscher, L., Van Zijl, P.: Mri atlas of human white matter. *American Journal of Neuroradiology* **27**(6), 1384 (2006)
16. Pawlowski, N., Glocker, B.: Is texture predictive for age and sex in brain mri? arXiv preprint arXiv:1907.10961 (2019)
17. Pominova, M., Artemov, A., Sharaev, M., Kondrateva, E., Bernstein, A., Burnaev, E.: Voxelwise 3d convolutional and recurrent neural networks for epilepsy and depression diagnostics from structural and functional mri data. In: 2018 IEEE International Conference on Data Mining Workshops (ICDMW). pp. 299–307. IEEE (2018)
18. Pominova, M., Kuzina, A., Kondrateva, E., Sushchinskaya, S., Burnaev, E., Yarkin, V., Sharaev, M.: Ensemble of 3d cnn regressors with data fusion for fluid intelligence prediction. In: Challenge in Adolescent Brain Cognitive Development Neurocognitive Prediction. pp. 158–166. Springer (2019)
19. Rescher, B., Rappelsberger, P.: Gender dependent eeg-changes during a mental rotation task. *International Journal of Psychophysiology* **33**(3), 209–222 (1999)
20. Selvaraju, R.R., Cogswell, M., Das, A., Vedantam, R., Parikh, D., Batra, D.: Grad-cam: Visual explanations from deep networks via gradient-based localization. *International Journal of Computer Vision* **128**(2), 336359 (Oct 2019). <https://doi.org/10.1007/s11263-019-01228-7>, <http://dx.doi.org/10.1007/s11263-019-01228-7>
21. Sharaev, M., Artemov, A., Kondrateva, E., Sushchinskaya, S., Burnaev, E., Bernstein, A., Akzhigitov, R., Andreev, A.: Mri-based diagnostics of depression concomitant with epilepsy: in search of the potential biomarkers. In: 2018 IEEE 5th International Conference on Data Science and Advanced Analytics (DSAA). pp. 555–564. IEEE (2018)
22. Spasojević, G., Stojanović, Z., Šušćević, D., Malobabić, S., Rafajlovski, S., Tatić, V.: Asymmetry and sexual dimorphism of the medial frontal gyrus visible surface in humans. *Vojnosanitetski pregled* **67**(2), 123–127 (2010)
23. Springenberg, J.T., Dosovitskiy, A., Brox, T., Riedmiller, M.: Striving for simplicity: The all convolutional net. arXiv preprint arXiv:1412.6806 (2014)
24. Suk, H.I., Lee, S.W., Shen, D., Initiative, A.D.N., et al.: Hierarchical feature representation and multimodal fusion with deep learning for ad/mci diagnosis. *NeuroImage* **101**, 569–582 (2014)
25. Tan, A., Ma, W., Vira, A., Marwha, D., Eliot, L.: The human hippocampus is not sexually-dimorphic: meta-analysis of structural mri volumes. *Neuroimage* **124**, 350–366 (2016)
26. Westerhausen, R., Walter, C., Kreuder, F., Wittling, R.A., Schweiger, E., Wittling, W.: The influence of handedness and gender on the microstructure of the human corpus callosum: a diffusion-tensor magnetic resonance imaging study. *Neuroscience letters* **351**(2), 99–102 (2003)
27. Xin, J., Zhang, X.Y., Tang, Y., Yang, Y.: Brain differences between men and women: Evidence from deep learning. *Frontiers in neuroscience* **13**, 185 (2019)
28. Zanto, Theodore P, G.A.: Fronto-parietal network: flexible hub of cognitive control. *Trends in cognitive sciences* **17**, 602–603 (2013)
29. Zhang, W., Li, R., Deng, H., Wang, L., Lin, W., Ji, S., Shen, D.: Deep convolutional neural networks for multi-modality isointense infant brain image segmentation. *NeuroImage* **108**, 214–224 (2015)